Article

The role of alkali metal cations and platinum-surface hydroxyl in the alkaline hydrogen evolution reaction

Aamir Hassan Shah ⓘ [1], Zisheng Zhang[1], Zhihong Huang[2], Sibo Wang ⓘ [1], Guangyan Zhong[1], Chengzhang Wan[1,2], Anastassia N. Alexandrova ⓘ [1] ✉, Yu Huang ⓘ [2,3] ✉ and Xiangfeng Duan ⓘ [1,3] ✉

The platinum-catalysed hydrogen evolution reaction (HER) generally shows poorer kinetics in alkaline electrolyte and represents a key challenge for alkaline water electrolysis. In the presence of alkali metal cations and hydroxyl anions, the electrode–electrolyte (platinum–water) interface in an alkaline electrolyte is far more complex than that in an acidic electrolyte. Here we combine electrochemical impedance spectroscopy and an electrical transport spectroscopy approach to probe and understand the fundamental role of different cations (Li^+, Na^+ and K^+) in HER kinetics. Our integrated studies suggest that the alkali metal cations play an indirect role in modifying the HER kinetics, with the smaller cations being less destabilizing to the hydroxyl adsorbate (OH_{ad}) species in the HER potential window, which favours a higher coverage of OH_{ad} on the platinum surface. The surface OH_{ad} species are highly polar and act as both electronically favoured proton acceptors and geometrically favoured proton donors to promote water dissociation in alkaline media, thus boosting the Volmer-step kinetics and the HER activity.

The HER is one of the most fundamental and critical reactions in renewable energy conversion and storage devices including electrolysers that convert and store intermittent renewable electricity in chemical form by producing hydrogen. On the other hand, the hydrogen oxidation reaction (HOR) plays a critical role in fuel-cell technologies that convert stored chemical energy into electricity. The HER/HOR mechanism and kinetics are drastically different in acidic and alkaline media[1,2]. Platinum (Pt) is a state-of-the-art electrocatalyst for these reactions, and thus significant efforts have been devoted to understanding the reaction mechanism and kinetics of Pt-based electrocatalytic systems[3–5]. Hitherto, various hypotheses have been proposed to identify and understand the reaction descriptors that account for the effect of pH on the HER on Pt electrode surfaces. It has been well recognized that the HER rate and mechanism are related to the strength of the hydrogen binding energy (HBE) of the metal. For example, on the basis of a density functional theory (DFT) database of hydrogen chemisorption energies, Nørskov et al. introduced the so-called volcano plot and confirmed that Pt represents an optimum HER catalyst, particularly in acidic environments[4].

Although the HBE of a pure metal surface can in principle serve as an effective physical descriptor for the HER, the experimental determination of the relevant physical parameters is often complicated by the presence of the electrolyte and different surface adsorbates, particularly in alkaline electrolytes where the adsorbates are more complex. For example, Yan and colleagues studied the HER in different pH-buffered electrolytes and suggested that a monotonic decrease in the HER activities by increasing the pH can be correlated with continuously strengthened electrochemical HBE values[6]. On the other hand,

[1]Department of Chemistry and Biochemistry, University of California, Los Angeles, CA, USA. [2]Department of Materials Science and Engineering, University of California, Los Angeles, CA, USA. [3]California NanoSystems Institute, University of California, Los Angeles, CA, USA. ✉e-mail: ana@chem.ucla.edu; yhuang@seas.ucla.edu; xduan@chem.ucla.edu
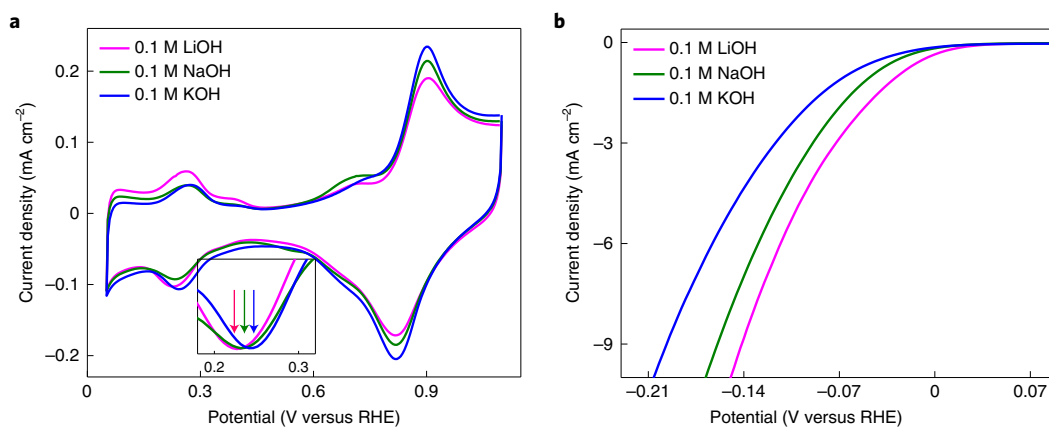
Fig. 1 | Voltammetric studies in alkaline electrolytes with different AM⁺.
a, Cyclic voltammograms on a stationary polycrystalline Pt disc electrode at a scan rate of 100 mV s⁻¹ (the inset shows an expanded view of the normalized H_{upd} peak). **b**, HER polarization curves (iR-corrected; i, current; R, resistance) collected at room temperature on a polycrystalline Pt disc electrode in N₂-saturated 0.1 M MOH (M = Li, Na and K) at a scan rate of 5 mV s⁻¹ with a rotation speed of 1,600 revolutions per min.

Koper and co-workers suggested that a positive shift in the peak for hydrogen underpotential deposition (H_{upd}) in cyclic voltammetry (CV) is not because of HBE changes but originates from destabilization of the OH_{ad} species on Pt(100) and Pt(110) sites by the presence of alkali metal cations near the interface[7,8]. Moreover, Koper and colleagues have also shown that the HBE descriptor cannot fully explain the pH-dependent catalytic behaviour on Pt(111), which shows significant pH-dependent HER kinetics but only a small dependence of the H_{upd} peak potential shift on the pH[9]. Thus, despite the undeniable success of the HBE in acidic media, it is not an unambiguous descriptor for HER/HOR kinetics in alkaline media, largely due to the more complex electrolyte environment and the elusive role of different surface adsorbates that may modify the interfacial molecular structures and reaction pathways.

Markovic and others ascribed the slower HER kinetics in alkaline media to the high energy barrier for H_2O dissociation compared with H_3O^+ in acidic media[10–12], and suggested that the HER kinetics in alkaline media can be improved by the presence of oxophilic groups that can stabilize OH_{ad}, which in turn facilitates H_2O dissociation[13]. Later, the same group observed a monotonic relationship between the HER activity and the OH_{ad} affinity of the oxophilic groups, and concluded that the HER activity follows the Brønsted–Evans–Polanyi principle to promote the HER kinetics; from this, they proposed a bifunctional mechanism in which the edges of oxophilic metal clusters (M(OH)₂) promote H_2O dissociation and the production of adsorbed hydrogen atoms (H_{ad}) on nearby Pt surfaces that then recombine into molecular hydrogen[14]. This bifunctional mechanism has been supported by a number of studies[15–18]. For example, Jia and co-workers experimentally verified the bifunctional mechanism through combined electrochemical and operando spectroscopic data[15], and robustly demonstrated that the presence of hydroxyl groups on surface Ru sites in the HOR potential region plays a key role in promoting the rate-determining Volmer step[15]. Moreover, McCrum and Koper recently investigated the further role of OH_{ad} on the HER activity in alkaline media, and demonstrated that the HER activity exhibits a volcano-type relationship with the hydroxyl binding strength, supporting the Brønsted–Evans–Polyani relationship[19].

In addition to the HBE and the bifunctional mechanism, Koper and co-workers suggested that the potential of zero free charge may play an important role[9]. In this picture, the HER/HOR region in acidic media is closer to the potential of zero free charge (~0.34 V_{RHE} (the voltage versus the reversible hydrogen electrode)), and the reorganization energy for interfacial water to move a proton through the electrical double layer (EDL) is smaller; by contrast, the HER/HOR region in alkaline media is far from the potential of zero free charge (~1.0 V_{RHE}, that is, closer to the OH_{ad} region) and the strong electric field in the HER/HOR region leads to a larger interfacial water reorganization energy that could limit the transfer of OH^- through the double layer[9].

Apart from the differences in these distinct theories and different levels of success in various aspects, none of them consider the effect of alkali metal cations (AM⁺) on the HER kinetics, which can hardly be ignored in alkaline electrolytes. For example, Markovic and co-workers observed that the HER activity on a Ni(OH)₂–Pt surface was promoted in the presence of Li⁺ cations, which they attributed to water dissociation[13]. Bandarenka and colleagues reported a similar promotion of the HER activity on a Pt electrode by AM⁺ (ref. [20]), and suggested that the cations may alter the HBE, thus altering the HER activity[20]. Jia and collaborators attributed the enhancement in HER activity to the presence of OH_{ad}–(H₂O)$_x$–AM⁺ in the double-layer region, which facilitates the removal/transport of OH_{ad} into the bulk, forming OH^-–(H₂O)$_x$–AM⁺ as per the hard–soft acid–base theory, thereby promoting the HER[16]. Koper and co-workers recently suggested a change in the rate-determining step from the Heyrovsky to the Volmer step in Li⁺- and K⁺-containing electrolytes, respectively[21]. Overall, although an enhancement of the HER activity on a Pt electrode in the presence of Li⁺ when compared with other larger AM⁺ has been consistently observed, a full understanding of this phenomenon has been a topic of considerable debate. Therefore, to more completely understand the descriptor that dictates the HER activity in alkaline media, it is essential to investigate how the different cations alter the local (on-surface or near-surface) chemical environment at the electrode–electrolyte interface.

Here we address this issue by systematically studying the influence of cations on the HER on a Pt surface in alkaline media. We observed that the HER activity in alkaline media is clearly dependent on the exact AM⁺ (Li⁺ > Na⁺ > K⁺), which is consistent with previous studies[20,22]. We further use a unique electrical transport spectroscopy (ETS) approach to probe the Pt-surface adsorbates directly at variable potentials, and electrochemical impedance spectroscopy (EIS) to study the near-surface environment in the EDL and the charge-transfer resistance (R_{ct}) at the electrode–electrolyte interface. On the basis of these comprehensive on-surface and near-surface signals, we conduct DFT calculations with explicit solvation, including static calculations, grand canonical DFT calculations, ab initio molecular dynamics (AIMD) simulations and micro-solvation molecular-cluster calculations to develop molecular-level insights into the surface-adsorption properties, solvation structure and the Pt–water interface dynamics in the presence of
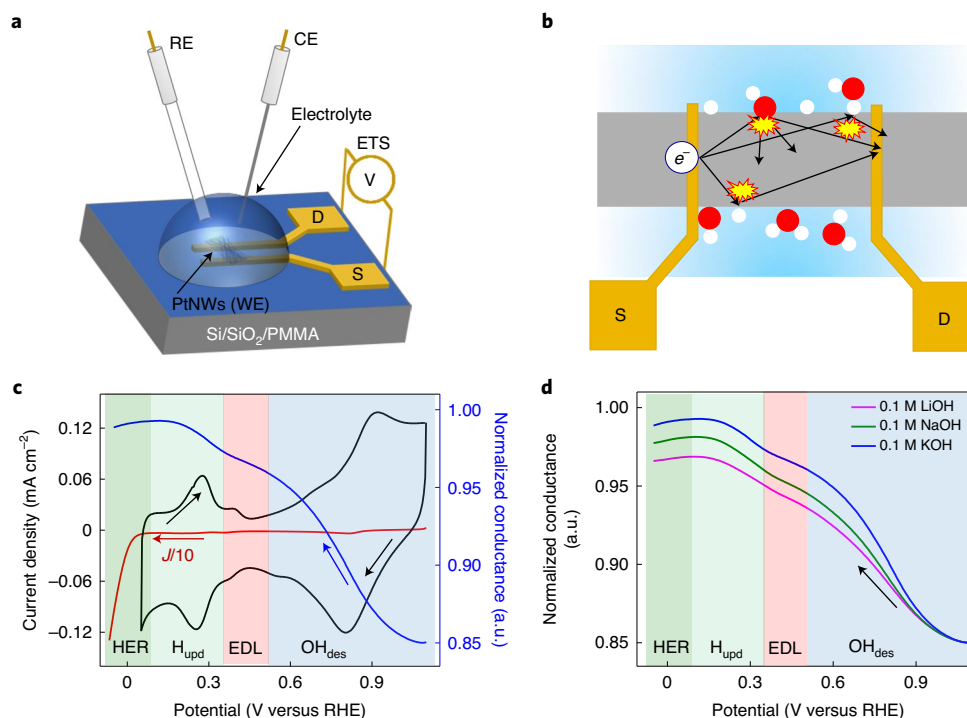
Fig. 2 | Schematic illustration and working principle of the ETS measurements. a, On-chip PtNW device for ETS measurements, where RE, CE and PtNWs (WE) are the reference, counter and working electrodes, respectively, and S and D represent the source and drain terminals, respectively. **b**, Electron-scattering mechanism of various adsorbate molecules (red and white colour represents O and H atoms respectively) on the PtNWs. **c**, Typical cyclic voltammogram (black), negative sweeping branch to the HER region (red) and ETS spectrum (blue). The red curve is divided by ten due to the much larger HER current in the HER potential window. The hydroxyl desorption (OH_{des}), EDL, H_{upd} and HER regions are highlighted with different background colours. **d**, Normalized ETS conductance signal versus potential of the PtNW device in 0.1 M MOH (M = Li, Na and K) electrolyte solutions with different AM^+.

cations and surface OH_{ad} species. Together, we experimentally and theoretically resolve the elusive role of AM^+ and demonstrate that AM^+ play an indirect role in modifying the adsorption strength and coverage of the hydroxyl species $\left(-OH_{ad@Li^+} > -OH_{ad@Na^+} > -OH_{ad@K^+}\right)$ under the H_{upd}/HER potential regime, where the higher OH_{ad} coverage with smaller AM^+ promotes the HER activity. Specifically, our integrated studies reveal that Li^+ cations destabilize OH_{ad} on the Pt surface least (compared with Na^+ and K^+) and help to retain more OH_{ad} that in turn act as both proton acceptors and donors to the nearby water molecules and thus facilitate the Volmer-step kinetics and the HER activity in alkaline media (similar to the bifunctional mechanism), as also confirmed via the greatly reduced charge-transfer resistance observed in EIS studies. Our direct experimental and theoretical evidences provide critical fundamental insights into how and why AM^+ influence the HER kinetics in alkaline media. This could enable an important vision for the design of future electrolysers with both improved energy efficiency and reduced cost.

Results

Cation-dependent HER activity and surface adsorbates

Using CV and linear sweep voltammetry (LSV) we first examined the influence of cations on the Pt disc electrode with a conventional three-electrode system in alkaline electrolytes at pH 13 with different AM^+ (Li^+, Na^+ and K^+). The cyclic voltammograms in the HER/HOR regime show that the H_{upd} peak exhibits a clear dependence on the specific AM^+ (Fig. 1a). The peak potential is more positive in 0.1 M KOH, followed by NaOH and LiOH (inset in Fig. 1a). A consistent and even more prominent trend has previously been observed on single-crystal Pt surfaces by Koper and co-workers[7,23] in which the H_{upd} peak was attributed not only to H adsorption but also to the replacement of OH_{ad} by H_{ad} (ref. [23]). Thus, our work is in agreement with the previous reports that

the negative peak shift with smaller AM^+ is an indication that Li^+ cations better stabilize (or lesser destabilize) OH_{ad} in the lower potential regime compared with Na^+ and K^+ cations. Linear sweep voltammograms demonstrate that the highest HER activity was observed in the case of Li^+ followed by Na^+ and K^+ cations (Fig. 1b), which is also consistent with previous studies[16,24].

To understand the impact of these different AM^+ on the surface adsorbates in the H_{upd}/HER regime, we next carried out ETS studies to probe the adsorbed species directly on the Pt surface. The ETS approach uses ultrafine Pt nanowires (PtNWs) as a model catalyst[25,26], and involves the concurrent measurement of the PtNW conductance during electrochemical studies at different electrochemical potentials (Fig. 2a) (see Methods and ref. [25] for the detailed working principle). The PtNWs (~2 nm in diameter) used in ETS studies show qualitatively similar CV and LSV results (Supplementary Fig. 1) with a consistent trend of AM^+ dependence to other types of Pt catalyst (for example, the Pt disc electrode).

Using the ETS approach, when the diameter (d) of the ultrafine PtNWs is smaller than the electron mean free path ($\lambda \approx 5$ nm)[27], their resistance is particularly dependent on the surface adsorbates due to surface-adsorbate-induced scattering of the conduction electrons, producing a resistance change according to equation (1)[25]:

$$\rho = \rho_0 \left(\left(\frac{1-p}{1+p}\right) \times \frac{\lambda}{d}\right)(d \ll \lambda) \qquad (1)$$

where ρ and ρ_0 are the resistivity of the one-dimensional PtNWs and the bulk metal, respectively, λ is the mean free path of the electron and p is a specularity parameter, which has a value ranging from 0 (for highly diffusive scattering) to 1 (completely specular scattering) (Fig. 2b)[27]. The different surface adsorbate modifies the specularity

value (p) and thus the resistance of the nanowires. It should be noted such surface scattering is wholly sensitive to the surface adsorbates and is not sensitive to the electrostatic or electrochemical potential. For example, previous studies have shown that a constant conductance at different electrochemical potentials is obtained when there is a stable surface-adsorbate layer (for example, CO or I$^-$) that does not change with potential[25,26], confirming the insensitivity of the metallic PtNWs to the varying electrochemical potential. Thus, the ETS approach offers a unique signal-transduction pathway to probe the surface adsorbates exclusively, with little interference from the electrochemical potential or the bulk electrolyte environment, which is difficult to achieve with other analytical approaches that are often convoluted with the near-surface (for example, EDL) or bulk electrolyte background. In addition, compared with interfacial-charge-transfer-based CV studies that cannot usually resolve the surface adsorbates during the active catalytic process (for example, in HER potential regime) due to the dominance of the much larger catalytic current over the surface-adsorbate charge transfer, ETS is wholly sensitive to the surface adsorbates and is insensitive to the catalytic current. Thus, the ETS approach can enable probing of the surface adsorbates of active catalytic surfaces in action, which is essential for deciphering catalytic molecular pathways.

We first closely compared the ETS measurements with the corresponding the CV curve when the potential was gradually changed from 1.10 to −0.05 V$_{RHE}$ (Fig. 2c) and four distinct regions were consistently shown: (1) the O/OH$_{ad/des}$ region (1.10–0.52 V$_{RHE}$); (2) the EDL region (in which OH$_{ad}$ is replaced by H$_2$O) (0.52–0.35 V$_{RHE}$); (3) the H$_{upd}$ regime (0.35–0.08 V$_{RHE}$); and (4) the HER regime (from 0.08 to −0.05 V$_{RHE}$). The lowest conductance observed in the high-potential regime is attributed to the larger scattering from the strongly bonded OH$_{ad}$ on the Pt surface, which significantly reduces the conductance of the PtNWs. Scanning the potential toward the lower potential regime results in a monotonic increase in conductance due to the gradual replacement of OH$_{ad}$ by H$_2$O. The conductance increase slowed in the double-layer regime where the Pt surface is nearly completely reduced and most of the OH$_{ad}$ are replaced by H$_2$O. Further sweeping of the potential to the more negative regime results in H$_{upd}$ on the electrode surface (replacement of surface-adsorbed H$_2$O and residual OH$_{ad}$ by H$_{upd}$), which further reduces the scattering and increases the conductance. The conductance eventually saturates at a nearly stable value below 0.15 V$_{RHE}$ (beyond the H$_{upd}$ peak in the CV curve) due to the high coverage of adsorbed hydrogen. The ETS conductance measurement retains the nearly saturated conductance well into the HER regime (0.08 to −0.05 V$_{RHE}$), suggesting a largely similar surface-adsorption status in the HER regime. The derivative of the ETS shows two peaks near the potential regime where most OH desorption and H adsorption occurs, which is largely consistent with the CV curve and further highlights the validity of our approach and analysis (Supplementary Fig. 2).

We further compared the ETS data obtained for the three different cations (Li$^+$, Na$^+$ and K$^+$). It was found the ETS data show essentially the same conductance in the high-potential regime (1.10–1.00 V$_{RHE}$), suggesting a similar hydroxyl adsorption state at such potentials. As we scan the potential towards the lower potential regime, a notable conductance increase is observed in all cases, following a largely similar trend. However, it is interesting to note that the conductance increase is less pronounced with a smaller slope in the case of Li$^+$ cations compared with that of Na$^+$ and K$^+$ (Fig. 2d). Considering that the conductance increase primarily results from the replacement of OH$_{ad}$ by H$_2$O and then by H$_{upd}$, the smaller increase in conductance in the presence of Li$^+$ cations suggests that fewer OH$_{ad}$ are being desorbed or replaced by H$_2$O or H$_{ad}$ compared with that of the other larger cations (Na$^+$ and K$^+$). We note that the difference among these three cations persist throughout the entire potential regime down to −0.05 V$_{RHE}$, suggesting that different amounts of OH$_{ad}$ remained on the Pt in the H$_{upd}$/HER potential window.

Theoretical insight into the role of cations on surface adsorbates

Although it has commonly been perceived that OH$_{ad}$ may not be stable in the H$_{upd}$/HER potential regime, there are occasional suggestions that some level of OH$_{ad}$ may persist at this potential range[7,8], which is consistent with our ETS studies. To understand these experimental findings, we performed theoretical studies to investigate the extent of OH$_{ad}$ in the presence of different cations. To gain insight into how and why different cations influence the surface-adsorption properties, DFT calculations were performed on the Pt(111)–water interface, which is modelled by the Pt(111) slab covered with an explicit water layer (Supplementary Fig. 3). The DFT-optimized geometries are shown in Supplementary Fig. 4. The adsorption energy of OH$_{ad}$ (E_{ad}^{OH}) on Pt(111) is calculated to be −3.46 eV, −2.81 eV and −2.32 eV in the presence of Li$^+$, Na$^+$ and K$^+$, respectively (Fig. 3a) (see below for estimation of the statistical fluctuations from solvent dynamics). Compared with the case of a pure water environment (−3.50 eV), the presence of cations destabilizes the OH$_{ad}$, and the extent of such destabilization follows the trend of K$^+$ > Na$^+$ > Li$^+$. Grand canonical DFT calculations (Fig. 3b) confirm that this trend persists for the potential-dependent adsorption free energy of OH (G_{ad}^{OH}) throughout the entire electrochemical window (−1.0 to 1.0 V$_{RHE}$), and that OH$_{ad}$ is favourable even under a more negative potential.

Our DFT calculations show that the adsorption strength of OH$_{ad}$ follows the order of Li$^+$ > Na$^+$ > K$^+$, which is consistent with the experimental observations in ETS studies (Fig. 2d). To understand the origin of such a difference in adsorption strength, we further calculated the electron density difference ($\Delta\rho_e$) at the Pt(111)–water interface after introducing different cations. Overall, the interaction between the cation and the OH$_{ad}$ is mostly electrostatic (decays via an inverse square law) and its effect on the electronic structure of the Pt surface is mild. The yellow isosurfaces between the cation and the nearby water molecules show the redistribution of the electron density on water to form the cation–water bonds, where a larger lobe indicates a higher extent of such redistribution (Fig. 3d–f). The more pronounced electron density redistribution in the presence of Li$^+$ can be attributed to the stronger local electric field from its higher charge density (that is, the same net charge but with a much smaller ionic radius) compared with Na$^+$ and K$^+$. The electric field exerted by the cation also causes redistribution of the electron density in the OH$_{ad}$, reducing the electron density of the lone pair closest to the cation (region A in each inset) while increasing for the farther lone pair (region B in each inset). It is interesting to note that the region corresponding to the Pt–O bond (region C in each inset) also experiences an increase in electron density, which is due to charge compensation from bulk Pt to the polarized OH$_{ad}$.

To quantify further such polarization and charge redistribution for OH$_{ad}$, we performed Bader charge analysis on the interface (Supplementary Fig. 5), and the net charge on O in OH$_{ad}$ is calculated to be −0.52 |e|, −0.49 |e| and −0.48 |e| in the presence of Li$^+$, Na$^+$ and K$^+$, respectively. Based on these Bader charges, the dipole moment of the O–H$_{ad}$ (Pt–O) bonds are calculated to be 2.37 D (2.09 D), 2.19 D (1.69 D) and 2.15 D (1.06 D) for Li$^+$, Na$^+$ and K$^+$, respectively (Fig. 3c). Hence, it is clear that the extent of charge redistribution and polarization for OH$_{ad}$ both follow the trend of Li$^+$ > Na$^+$ > K$^+$, which is probably caused by the stronger electric field of Li$^+$, analogous to polarization of the first hydration sphere.

Since the hydration sphere and water configuration at the Pt–water interface are not static, we further performed AIMD simulations at the Pt(111)–water interface with near-surface hydrated cations in the canonical ensemble at 300 K to account for the dynamics and to better sample the configurational space. A 100 ps trajectory is obtained for each system after pre-equilibration, with a variance of potential energy within 0.15 eV, marking proper equilibration of the system (Supplementary Fig. 6). The cation–oxygen radial distribution function (RDF; $g_{cation-O}(r)$) data (Supplementary Fig. 7) obtained from the AIMD trajectory simulations are consistent with the results of large-scale molecular
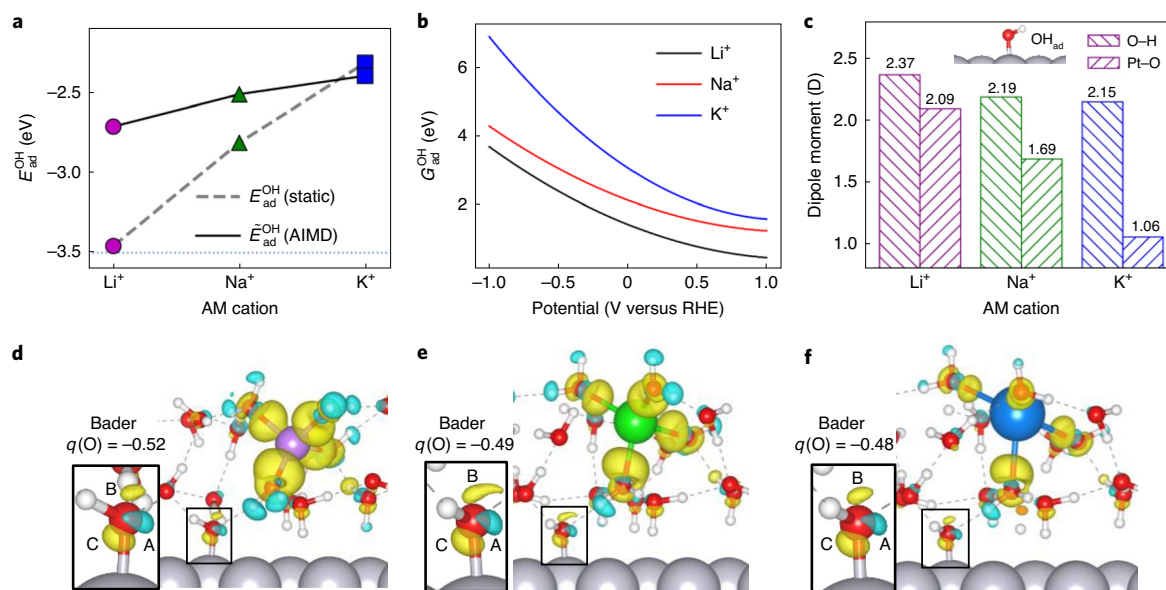
Fig. 3 | Effect of cations on the adsorption of OH at the Pt(111)–water interface. a, Adsorption energy of OH (E_{ad}^{OH}) in the presence of Li$^+$, Na$^+$ and K$^+$ from static calculations and AIMD simulations (the statistical spread is omitted here for clarity–see Supplementary Information). The dotted horizontal line marks the adsorption energy in the absence of any cation. **b**, The potential-dependent G_{ad}^{OH} in the presence of Li$^+$, Na$^+$ and K$^+$ in the potential window of 1.0 V$_{RHE}$ to –1.0 V$_{RHE}$. **c**, Bar plot showing the dipole moment of OH$_{ad}$ based on

Bader charges. **d–f**, Electron density difference maps of the Pt(111)–OH$_{ad}$–water interface after introducing Li$^+$ (**d**), Na$^+$ (**e**) and K$^+$ (**f**) plotted at the isovalue of 0.0025 electrons Å^{-3}. Yellow and cyan isosurfaces represent spatial regions experiencing an increase or decrease in electron density, respectively. The insets are expanded views of the OH$_{ad}$ regions, with the key isosurfaces and Bader charges on O (q(O), in |e|) labelled.

mechanics simulations[28] and test simulations with a larger cell size or thicker water layer (Supplementary Note 1), demonstrating the correct hydration structure of the cations. The adsorption enthalpy (approximated by the molecular dynamics average of potential energy) of OH ($\tilde{E}_{ad}^{OH}$) is calculated to be –2.71 eV, –2.51 eV and –2.40 eV in the presence of Li$^+$, Na$^+$ and K$^+$, respectively (Fig. 3a), which is largely consistent with the trend of E_{ad}^{OH} and potential-dependent G_{ad}^{OH} calculated for static models (Fig. 3a,b), further confirming more the favourable OH$_{ad}$ in the presence of Li$^+$.

The reduction of the adsorption energy (Fig. 3a) with increasing AM$^+$ size (from Li$^+$ to Na$^+$ to K$^+$) is contributed by the interface dynamics. We note it has been a debated topic as to whether the cations adsorb directly or simply accumulate in the outer-Helmholtz plane in the double layer[29–31]. Hence, we further studied the cation dynamics and the hydration structure. The representative snapshots of each system at equilibrium and at the position closest to the surface (Supplementary Fig. 8) show that the cation stays in the double layer most of the time, oscillating between the first and second water layers. During the 100 ps AIMD simulations, Li$^+$ maintains a coordination number (CN) of 4 and oscillates in the upper half between the first and second water layers. The CN fluctuates between 4 and 5 for Na$^+$ and oscillates in the lower half between the first and second water layers. By contrast, K$^+$ does not have a specific CN and frequently penetrates the first water layer but never stays specifically adsorbed on the Pt surface. The cation CN values (4 for Li$^+$, ~4–5 for Na$^+$ and ~4–6 for K$^+$) obtained in our simulations are consistent with ref. [32], and the position of the cations is consistent with ref. [31]. The average distance between the cation and the Pt(111) surface for Li$^+$, Na$^+$ and K$^+$ is, respectively, 4.44 Å, 4.42 Å and 3.95 Å without surface OH and 5.38 Å, 4.43 Å and 3.88 Å with surface OH, which is due to the different rigidity of their hydration spheres as also characterized by the sharpness of the RDF peak (Supplementary Fig. 7). Notably, only Li$^+$ is observed to have a well-defined second hydration sphere, and only K$^+$ experiences instantaneous penetration of water inside its first hydration shell (Supplementary Fig. 7). The variation in the cation-surface distance partially smears the difference in OH adsorption for different

cations, while leaving the overall trend qualitatively unchanged. The distinct interfacial dynamics are attributed to the different charge density of the cations, the cation–water interaction strength and the mass of the cations (heavier cations are less dragged by the friction of their water environment). It is noted that the observation that the cations do not stay dehydrated and form bonds with the Pt surface contradicts the hypothesis previously proposed in refs. [7,30,33,34], the discrepancy of which is probably the result of undercoordination of the cations through insufficient explicit solvation, which leads to an overestimation of the cation–surface binding strength. We also note that previous studies indicated that large cations (for example, Cs$^+$) may show a stronger interaction and direct adsorption on the electrode surface due to their less tightly bound solvation shell[24]. Indeed, our preliminary ETS studies also suggested that larger cations (Rb$^+$ or Cs$^+$) may directly adsorb on the electrode surface (Supplementary Note 2) and are expected to influence the HER activity in a very different way. Therefore, we excluded Rb$^+$ and Cs$^+$ ions from this study.

Cation modulation of the local chemical environment and HER kinetics

The aforementioned experimental ETS results and theoretical calculations confirm that the AM$^+$ do not specifically adsorb on the electrode surface but instead accumulate in the outer-Helmholtz plane. To probe the distribution of cations in the outer-Helmholtz plane of the EDL, we performed EIS analyses in different cation electrolytes and determined the double-layer capacitance (C_{dl}) at different applied potentials (Fig. 4a). In the simplified equation (2), the C_{dl} is directly related to the relative permittivity (ε) of the solvent at a constant electrolyte concentration (C), as well as the vacuum permittivity (ε_0), as shown below[35]:

$$C_{dl} = \varepsilon \varepsilon_0 \sqrt{C}. \qquad (2)$$

The EIS studies reveal a larger C_{dl} in the high-potential regime (1.1–0.6 V$_{RHE}$) for K$^+$ than for Na$^+$ and Li$^+$, which can be attributed to the lower hydration energy, the shorter cation–surface distance and the less
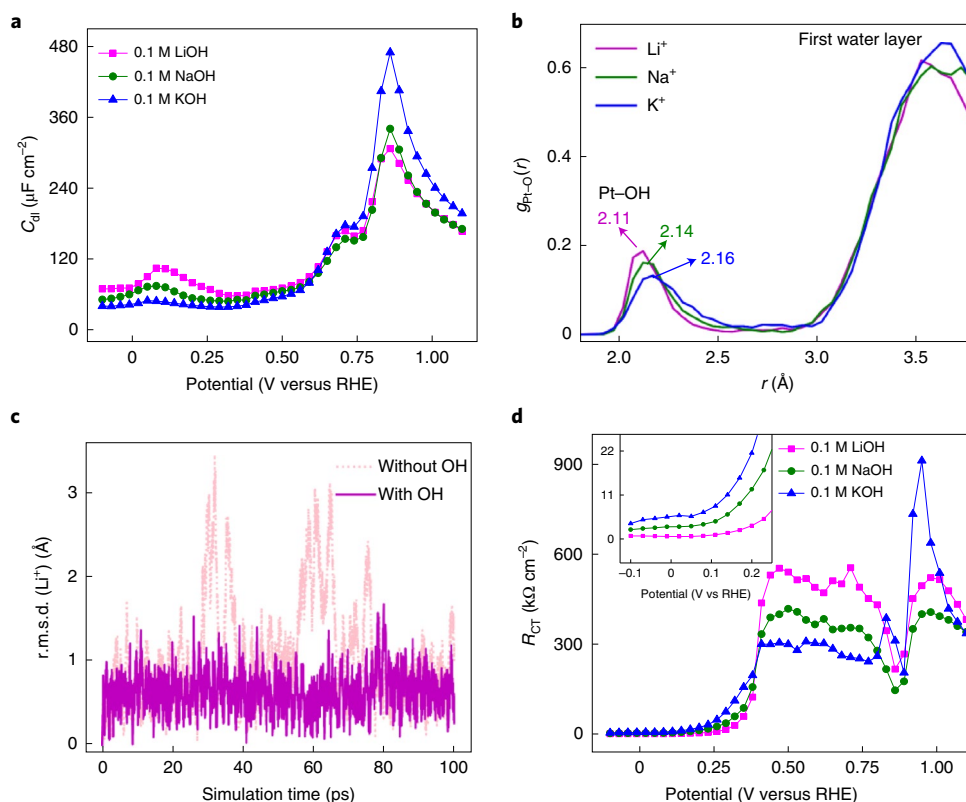
Fig. 4 | EIS and DFT investigation of the role of OH$_{ad}$. a, Double-layer capacitance (C_{dl}) on the Pt disc electrode at different applied potentials in 0.1 M MOH solutions (M = Li, Na and K). **b**, The RDF $g_{Pt-O}(r)$ between Pt and O atoms at the Pt(111)−OH$_{ad}$−water interface in presence of Li$^+$, Na$^+$, and K$^+$ ions calculated from AIMD trajectory. r, distance between Pt and O atom. **c**, The r.m.s.d. of the position of Li$^+$, with and without OH$_{ad}$ on the Pt surface, during the 100 ps AIMD simulations. **d**, Charge-transfer resistance (R_{ct}) on the Pt disc electrode at different applied potentials in 0.1 M MOH solutions (M = Li, Na and K).

rigid hydration sphere (and hence a smaller effective hydration-sphere radius) of K$^+$ compared with Na$^+$ and Li$^+$ (ref. [36]). However, an opposite trend was observed when the potential entered the H$_{upd}$/HER regime, with a larger C_{dl} shown in the case of Li$^+$. This reversal in C_{dl} is attributed to the change in the local cation concentration induced by the change in surface species. With the interaction between the hydrated cation and surface OH$_{ad}$ shown in our DFT calculations, we hypothesize that the local cation concentration may be highly dependent on the coverage and polarity of the surface OH$_{ad}$, and may be substantially different from the bulk concentration.

To explore further how the surface OH$_{ad}$ and near-surface cations influence the dynamic properties of each other, we analysed the AIMD trajectories of the Pt(111)−water and Pt(111)−OH$_{ad}$−water interfaces with near-surface hydrated cations. The first peak in the RDF of Pt−O (Fig. 4b) corresponds to the Pt−OH bond, and is the leftmost and the sharpest in the presence of Li$^+$, followed by Na$^+$ and K$^+$, suggesting that the strongest Pt−OH bond is with Li$^+$, which is consistent with the experimental and theoretical results discussed in the previous sections. The second peak corresponds to the first water layer, which it is about the same distance for the three cations, showing the consistent distribution of near-surface water that is independent of the identity of the hydrated cation.

Interestingly, the polarized OH$_{ad}$ in turn could stabilize the hydrated cation to stay in its surroundings. The root mean squared deviation (r.m.s.d.) of the Li$^+$ position from the Pt surface shows a considerably larger fluctuation in the absence of OH$_{ad}$ (Fig. 4c), suggesting the large and frequent oscillation and the drifting of Li$^+$ away from its equilibrium position (zero reference). After introducing OH$_{ad}$, the r.m.s.d. flattens and seldom goes beyond 1.5 Å from the equilibrium position, suggesting the anchoring of Li$^+$ cations to the Pt surface by

OH$_{ad}$. A similar anchoring effect is also observed for Na$^+$ and K$^+$ ions, although to a lesser extent due to the weaker cation−OH interactions (Supplementary Fig. 9). We note that such anchoring differs from the specific adsorption since the cation and OH$_{ad}$ are separated by the first hydration shell (~4 Å apart) without forming any direct cation−OH bond or OH$_{ad}$-induced dehydration (Supplementary Note 3), which differs from the work by the group of Koper and Janik despite a similar trend[7,8]. Since the OH$_{ad}$ has the highest surface coverage and polarity in the presence of Li$^+$, followed by Na$^+$ and K$^+$, this means more anchors and a stronger anchoring effect, leading to a higher local concentration of cations (Li$^+$ > Na$^+$ > K$^+$) near the Pt surface.

To conclude, the crossover of C_{dl} in the EIS results near 0.60 V$_{RHE}$ is induced by the change in the surface coverage of OH$_{ad}$: (1) at a higher potential (>0.60 V$_{RHE}$) where there are abundant surface OH$_{ad}$ species, the capacitance (K$^+$ > Na$^+$ > Li$^+$) is more determined by the inverse of the cation−surface distance and the hydration-sphere size; and (2) at a lower potential (<0.60 V$_{RHE}$) when there is only a limited number of OH$_{ad}$ species, the capacitance (Li$^+$ > Na$^+$ > K$^+$) is more dictated by the local cation concentration, which is in turn related to the coverage of remaining OH$_{ad}$ due to its anchoring effect.

The charge-transfer resistance was also determined from the EIS data. The electrode−electrolyte interface was largely capacitive over the entire potential range except for the HER region (Fig. 4d). The charge-transfer resistance in the oxidation region (~1 V) is not meaningful as it is largely capacitive with a minimal charge-transfer process. However, in the hydroxyl-desorption potential regime (~0.9−0.4 V$_{RHE}$), the charge-transfer resistance is larger for Li$^+$ ions when compared with Na$^+$ and K$^+$ ions, suggesting the more difficult desorption of OH$_{ad}$ and replacement by H$_2$O molecules in the presence of Li$^+$ ions, which is consistent with our ETS results. By contrast, in the H$_{upd}$ and HER
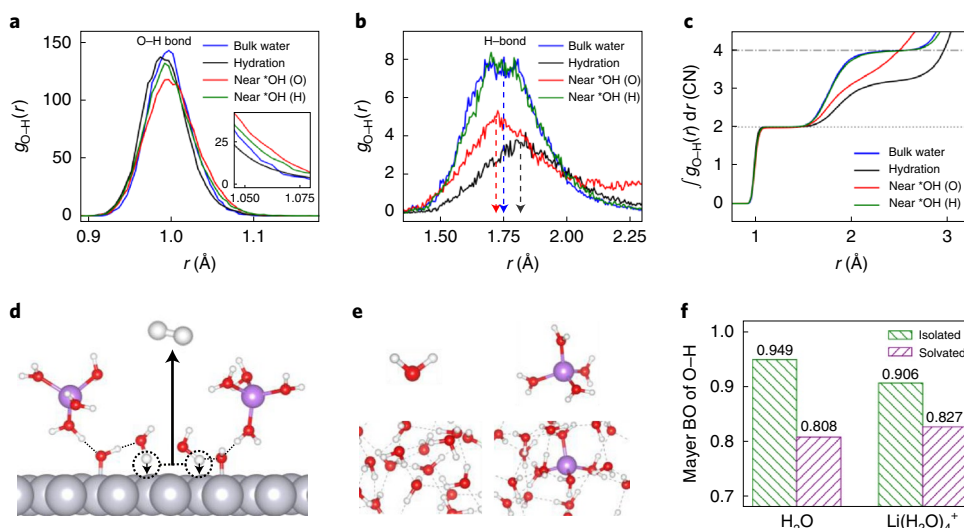
Fig. 5 | AIMD and micro-solvation simulations of cation and OH$_{ad}$. a,b, The RDF $g_{O-H}(r)$ between O and H atoms of the Pt(111)−OH$_{ad}$−water interface in the presence of Li$^+$ in the covalent O−H region (**a**) and the non-covalent O···H hydrogen-bond region (**b**). The different curves belong to water molecules in the hydration sphere of Li$^+$, in bulk water or near the surface OH$_{ad}$ as its hydrogen-bond donor or acceptor. The inset in **a** shows an expanded view of the tail region corresponding to O−H stretching. **c**, Integrated $g_{O-H}(r)$ showing the CN of O by H at different r(O−H) distances, with dotted and dash-dot lines marking CN = 2 and CN = 4, respectively. **d**, Schematic showing the promotion of the alkaline Volmer step by surface OH$_{ad}$ at the Pt(111)−water interface. **e**, Optimized geometry of H$_2$O and Li(H$_2$O)$_4^+$ in the isolated state (top row) and in the solvated state (bottom row). **f**, Bar chart of the Mayer bond order (BO) of O−H in H$_2$O and Li(H$_2$O)$_4^+$ in the isolated state and in the solvated state.

regimes (<0.4 V$_{RHE}$), the charge-transfer resistance is the lowest for Li$^+$ ions, followed by Na$^+$ and K$^+$ ions, which consistent with the improved Volmer-step kinetics for H$_{upd}$ and HER for Li$^+$ ions followed by Na$^+$ and K$^+$ ions (Fig. 1b).

To further understand the HER activity trend, we focused on the behaviour of water molecules in the AIMD because water is the major proton source in the alkaline HER. With the alkaline Volmer step (involving water dissociation) being the rate-determining step[13], the O−H bond strength in near-surface water could work as a metric to explain the HER activity. To this end, we examined the RDF of O−H of water with different surrounding species (Fig. 5a). Compared with water in the regular bulk water environment, the water O−H bond length in the first hydration shell of the cation experiences a downshift in the peak position and a slight sharpening of the peak, suggesting the strengthening of the O−H bond of water in the hydration shell of the cation. On the other hand, the O−H peak of a water molecule next to both O and H of OH$_{ad}$ show a longer tail on the stretching side (~1.05–1.1 Å), indicating that OH$_{ad}$ can function as both a proton acceptor and donor to weaken the O−H bond in nearby water, hence leading to a lower barrier for water dissociation.

The variation in water reactivity near different species can also be partly explained via the different hydrogen-bond strengths with their environment, which is characterized by the hydrogen-bond peak in the O···H RDF. The earlier and sharper peaks in the $r \approx$ 1.5–2.0 Å region (Fig. 5b) suggest stronger and more directional hydrogen-bond interactions on the water molecules by its environment. Compared with the bulk water case (peak position at ~1.76 Å), the water in the first hydration shell of the cation has a broader shape and later peak position (~1.80 Å) due to the blockage/restraint of hydrogen-bond formation through the steric arrangement of the cation and the hydration shell. It is interesting to note the water molecules near the O in OH$_{ad}$ show a shorter hydrogen-bond peak (~1.73 Å), indicating a considerably strengthened hydrogen bond, which fundamentally originates from the highly polar OH$_{ad}$ with a much higher negative charge density on O atoms than that in the near-surface water, as indicated by the Bader charges (−0.52 |e| on O in OH$_{ad}$ compared with around −0.2 |e| on O in near-surface water) (Supplementary Fig. 5a). These analyses indicate that the OH$_{ad}$ species function as strongly polarized H$^+$ acceptors for

nearby water molecules and thus facilitate water dissociation. The peak area, which corresponds to the CN of O by H (Fig. 5c), is smaller than the case of bulk water, probably due to the blockage of hydrogen-bond sites by the steric hindrance of the Pt surface.

The water near the H in OH$_{ad}$ (with OH$_{ad}$ being a hydrogen-bond donor) has a similar peak height/area to that in bulk water (Fig. 5b), indicating a similar hydrogen-bond strength. The Bader charge analysis indicates that there is a less positive charge on H in OH$_{ad}$ (0.04 |e| for H in OH$_{ad}$ versus ~0.1 |e| on H in water), and the surface OH$_{ad}$ is thus an electronically weaker hydrogen-bond donor. On the other hand, the longer tail in the O−H stretching region for water near H in OH$_{ad}$ (Fig. 5a inset) indicates that OH$_{ad}$ does function as a proton donor to weaken O−H in nearby water molecules, which is probably due to the synergistic geometric effect of the surface-bound OH$_{ad}$ and near Pt-surface water dynamics.

Together, by combining systematic experimental and theoretical studies, we reveal that the cations play an indirect role in the alkaline HER on Pt. It is the enhanced surface coverage of OH$_{ad}$ that is induced by the presence of smaller cations (Li$^+$), instead of the cation itself, that enhances the HER activity in alkaline media (Fig. 5d). The smaller cations lead to a higher OH$_{ad}$ coverage on the Pt surface in the HER potential window, and the OH$_{ad}$ can act as electronically favoured proton acceptors and geometrically favoured proton donors to promote water dissociation and the Volmer-step kinetics in alkaline media. The higher OH$_{ad}$ coverage in the case of Li$^+$ ions (followed by Na$^+$ and then K$^+$) leads to the higher HER activity.

We note in our findings that cations stabilizing their first hydration shell is in stark contrast to the common perception that the cations can directly activate the hydration sphere[33,37], and hence we performed a sanity check using a finer micro-solvation model at a higher level of theory and evaluated the Mayer bond order of the O−H bonds based on DFT-optimized geometries (Fig. 5e,f). Without explicit solvation, the Mayer bond order of O−H in the hydration shell of Li$^+$ (0.906) is lower than that of isolated water (0.949), which results from polarization by the electrostatics of the cation. Interestingly, the trend is reversed when the system is subject to explicit solvation. In a hydrogen-bond network, each water molecule is connected to four neighbouring water

molecules via hydrogen bonds, which causes a significant weakening of the O–H bond in water to result in a Mayer bond order of 0.808. However, each water molecule in the first hydration shell of Li$^+$ can only connect to two or three neighbouring water molecules due to the blockage of hydrogen-bond sites by the steric effect of the cation. The Mayer bond order of the O–H in the hydration shell of the cation (0.827) is therefore weakened to a lesser extent since the effect of the water environment outcompetes the effect of the cations. In other words, the water in the hydration shell of the cation is stabilized compared with the water in bulk water. Hence, the argument that a cation activates its hydration sphere is probably the result of underestimating the role of the water environment. We recognize that the models adopted in this study have certain limitations from various aspects due to computation–cost limitations (see Supplementary Note 4), and we believe that this example highlights well the necessity of including sufficient explicit solvation to properly describe the reactivity of water in both the bulk solution and at an electrochemical interface.

Conclusions

In conclusion, we have combined a unique surface-adsorbate specific ETS approach with EIS experiments and DFT calculations to directly probe the on-surface and near-surface chemical environment, deciphering the elusive role of AM$^+$ on Pt-surface chemistry and the alkaline HER. Our integrated studies suggest that the cation is not directly bonded to the Pt surface or OH$_{ad}$ but is separated by a water molecule in the first hydration shell of the cation, which is distinct from previous studies[7]. Moreover, smaller cations favour a higher OH$_{ad}$ coverage on the Pt surface in the HER potential window, where the OH$_{ad}$ in turn function as electronically favoured proton acceptors or geometrically favoured proton donors to promote water dissociation and Volmer-step kinetics on the Pt surface in alkaline media, leading to improved HER activity in the presence of smaller cations (Li$^+$). Our studies resolve the fundamental role of AM$^+$ in the HER kinetics, which has remained elusive in recent decades, and could offer valuable insights for the design of more efficient electrolysers for renewable energy conversion.

Methods

Chemicals

Lithium hydroxide (LiOH; >98%), sodium hydroxide (NaOH; 98%), potassium hydroxide (KOH; 87.4%) and perchloric acid (70%, PPT grade) were all purchased from Thermo Fisher Scientific. All aqueous solutions were prepared using deionized water (18.2 MΩ cm) obtained from an ultrapure purification system (Aqua Solutions).

Electrochemical measurements

All of the electrochemical measurements were performed using a typical three-electrode setup. A Pt rotating disc was used as the working electrode, and Pt wire and Ag/AgCl were used as the counter and reference electrodes, respectively. All of the potentials reported are versus the RHE, calibrated in the same electrolyte by measuring the potential of the HOR/HER currents at zero corresponding to 0 V$_{RHE}$.

Impedance measurements

The impedance spectra were measured using frequencies from 10^5 to 1 Hz with an amplitude of 10 mV$_{rms}$ at different applied voltages. Cyclic voltammograms were conducted between each potential point in the EIS measurement to avoid any influence from surface passivation. Equivalent circuits were fitted to the data using AfterMath software version 1.6.10513.

Synthesis of PtNWs

The PtNWs for the ETS measurements were synthesized following a previously reported protocol[38]. Briefly, Pt(acac)$_2$ (ac = acetylacetonate) (20 mg), Ni(acac)$_2$ (30 mg), W(CO)$_6$ (1.6 mg), glucose (135 mg) and 60 mg of polyvinylpyrrolidone (MW 40,000) were dissolved in 1-octadecene (2 ml) and oleylamine (3 ml). After sonicating for 15 min, the solution was sealed with argon. The mixture was then heated to 140 °C for 4 h. The product was centrifuged with ethanol for 15 min, followed by cyclohexane for 20 min. Finally, the product was centrifuged in a mixture of cyclohexane (5 ml) and ethanol (15 ml) for 20 min. The final product was dispersed in ethanol for device preparation.

Preparation of PtNW films

A free-standing PtNW film was assembled on-chip from the as-prepared PtNW suspension using a co-solvent evaporation method[25]. Briefly, the PtNW suspension in ethanol (400 μl, 0.4 mg ml^{-1}) was added dropwise into a beaker (about 9 cm in diameter) filled with deionized water. The thin film of PtNWs from the top of the water surface was then transferred onto the device.

Fabrication of the PtNW electrochemical device

The device fabrication followed an approach similar to that previously reported by our group[25]. Typically, a poly(methyl methacrylate) (PMMA; A8, MicroChem) film was prepared via spin coating onto the surface of the substrate (p^{++} silicon wafer with 300 nm thermal oxide) with pre-patterned Au electrodes (Ti/Au, 50/50 nm). E-beam lithography was then used to open windows on the PMMA, which created the desired patterns on the substrate. After removal of the PMMA template, PtNWs were deposited on the device substrate with the desired patterns. To rule out the influence of the electrolyte and to avoid electrochemical reactions on the Au electrodes, another layer of PMMA (~500 nm thick, electrochemically inert) was then deposited on the PtNW device via spin coating. A smaller window that only exposed PtNWs was opened using e-beam lithography. The device was finally used for in-device electrochemistry and in situ ETS measurements.

In-device CV and in situ ETS

A two-channel source/measure unit (SMU; Agilent B2902a) was used for the measurements. The first SMU channel was used as a potentiostat to control the potential of the source electrode compared with the reference electrode (V_G), while collecting the current (I_G) through the counter electrode at a scan rate of 50 mV s^{-1}. An SR830 lock-ln amplifier (Stanford Research Systems) was used to supply a small sinusoidal current (10 μA) between the source and drain electrodes and for collecting the corresponding source–drain voltage (V_{SD}). The source–drain voltage was then used to measure the conductance.

Slab model setup and DFT methods

The Pt–water interface is modelled using a Pt(111) slab and an explicit water slab on top of it. The Pt slab is a three-layer 4 × 4 supercell of Pt(111) termination with an area of 1.10 nm^2. The explicit water slab is 6 Å thick, and contains 22 water molecules (estimated from the water density of 1.0 g cm^{-3} at room temperature). The bottom two layers of the Pt slab are constrained as the bulk region, and everything else is allowed to relax as the interface region. A vacuum slab of 10 Å thickness was added in the Z direction to avoid spurious interactions between periodic images.

The solvation configuration for the production run was sampled through the random placement of water molecules in the water-slab region followed by local optimization at the DFT level, with a sampling size of 50 configurations, using our open-source Python package GOCIA (https://github.com/zishengz/gocia). The cation is introduced by replacing a water molecule and then re-optimizing the geometry. The surface OH$_{ad}$ is introduced by placing an OH species onto the Pt surface and then re-optimizing the geometry. Although our calculations use Pt(111) as the model system, we expect a similar conclusion to hold true for other surfaces, and it is noted that the stepped surfaces have even more favourable OH$_{ad}$ compared with the Pt(111) terrace[19].

The geometry optimizations were performed using the Perdew–Burke–Ernzerhof functional[39] and projector augmented-wave pseudopotentials[40] with the Vienna ab initio simulation package

program (version 5.4.1)[41–44]. D3 correction was used to better account for the dispersion interactions[45]. The convergence criteria for geometry (self-consistent field) are set to 10^{-5} eV for energy and 0.02 eV Å^{-1} for forces. Due to the relatively large system and sampling size, only the Γ k-point is sampled in the reciprocal space of the Brillouin zone throughout, and the cutoff energy for the kinetic energy of the plane waves was 400 eV. The Bader charges are calculated from the charge density output using Bader Charge Analysis code[46].

Grand canonical DFT calculations
Under a constant applied potential, the electrode surface is effectively a grand canonical ensemble where the number of electrons is varied to adapt to the change in the work function of the surface (caused by adsorbates or near-surface species). The potential-dependent electronic free energy of the surface ($G(U)$) can be approximated using the surface-charging method[47]:

$$G(U) = E(U) - q(U)FU \approx E(U_0) - \frac{1}{2}C(U - U_0)^2. \qquad (3)$$

Here, $E(U)$ is the electronic energy of the surface under a potential U, which is calculated by referencing the Fermi level of the system against the vacuum level; $q(U)$ is the surface charge difference referenced against the neutral system, and F is the Faraday constant; U_0 is the potential of zero charge in the vacuum scale, and C is the effective capacitance of the electrochemical interface. By varying the number of electrons in the system, the $E(U)$ of the system at the corresponding U and $q(U)$ can be obtained, and thereby a parabolic relationship between $G(U)$ and U can be fitted by sampling a series of q values. The U (in the vacuum scale) can be converted to the RHE scale by referencing it against the experimental U_{SHE} (standard hydrogen electrode, 4.44 V)[48] and adding a pH correction of 0.0592 × pH.

AIMD simulations
The AIMD simulations are performed on the optimized structures using the same DFT setting as for the geometry optimization using the VASP program (version 5.4.1). The simulations were performed in the *NVT* (canonical) ensemble at 300 K using the Nosé–Hoover thermostat. The time step was set to 1 fs, and the 100 ps trajectory after the equilibration of the system was collected for analysis. Multiple independent simulations starting with different cation height values were performed, and we observed little dependence of the obtained equilibrium on the initial conditions. The RDF analysis was performed using the VMD program (version 1.9.4a48)[49].

Calculation of adsorption energies
The adsorption energy of OH on the surface to form OH$_{ad}$ is calculated using

$$E_{ad}^{OH} = E(*OH_{ad}) - E(*) - E(OH). \qquad (4)$$

Here, the energy E is from the static calculation on a single configuration; the symbol $*$ denotes the Pt–water interface, and OH denotes an isolated OH species (via implicit solvation calculation or experimentally determined solvation free energy, see Supplementary Note 5).

The static DFT energy E can be replaced by the trajectory-averaged potential energy $\bar{E}$ from the AIMD simulation to yield the trajectory-averaged adsorption enthalpy:

$$\bar{E}_{ad}^{OH} = \bar{E}(*OH_{ad}) - \bar{E}(*) - E(OH). \qquad (5)$$

We can also replace E with the potential-dependent free energy $G(U)$ to yield the potential-dependent free energy of adsorption:

$$G_{ad}^{OH}(U) = G(U; *OH_{ad}) - G(U; *) - E(OH). \qquad (6)$$

Micro-solvation model setup and DFT methods
The isolated forms of the hydrated cations are Li(H$_2$O)$_4^+$, Na(H$_2$O)$_5^+$ and K(H$_2$O)$_6^+$, which are the typical hydration structures taken from ref. [32]. The outer-shell solvation configuration around the water and hydrated cations is sampled as a micro-solvation molecular cluster via the random placement of water molecules within a spherical region of 7 Å radius (around the species to be solvated) followed by local optimization at the DFT level, with a sample size of 50 configurations, using the Genmer module in the Molclus program[50].

The geometry optimizations were performed using the B3LYP functional[51,52] and def-TZVP basis sets[53] using the Gaussian 16 program[54] (Revision C.01). D3 correction[45] with Becke–Johnson damping[55] was used to better account for the dispersion interactions. Hirshfeld population analysis and Mayer bond order analysis were performed using the Multiwfn program[56] on the converged wavefunctions from DFT calculations.

Data availability
The data that support the plots within this paper and other findings of this study are available from the corresponding author upon reasonable request. The DFT-optimized geometries and AIMD trajectories are available in the Zenodo data repository at https://doi.org/10.5281/zenodo.7026971.

References
1. Sheng, W., Gasteiger, H. A. & Shao-Horn, Y. Hydrogen oxidation and evolution reaction kinetics on platinum: acid vs alkaline electrolytes. *J. Electrochem. Soc.* **157**, B1529–B1536 (2010).
2. Li, L., Wang, P., Shao, Q. & Huang, X. Recent progress in advanced electrocatalyst design for acidic oxygen evolution reaction. *Adv. Mater.* **33**, 2004243–2004266 (2021).
3. Gasteiger, H. A., Panels, J. E. & Yan, S. G. Dependence of PEM fuel cell performance on catalyst loading. *J. Power Sources* **127**, 162–171 (2004).
4. Nørskov, J. K. et al. Trends in the exchange current for hydrogen evolution. *J. Electrochem. Soc.* **152**, J23–J26 (2005).
5. Zhang, W. et al. WO$_x$-surface decorated PtNi@Pt dendritic nanowires as efficient pH-universal hydrogen evolution electrocatalysts. *Adv. Energy Mater.* **11**, 2003192–2003198 (2021).
6. Sheng, W., Myint, M., Chen, J. G. & Yan, Y. Correlating the hydrogen evolution reaction activity in alkaline electrolytes with the hydrogen binding energy on monometallic surfaces. *Energy Environ. Sci.* **6**, 1509–1512 (2013).
7. Chen, X., McCrum, I. T., Schwarz, K. A., Janik, M. J. & Koper, M. T. M. Co-adsorption of cations as the cause of the apparent pH dependence of hydrogen adsorption on a stepped platinum single-crystal electrode. *Angew. Chem. Int. Ed.* **56**, 15025–15029 (2017).
8. McCrum, I. T., Chen, X., Schwarz, K. A., Janik, M. J. & Koper, M. T. M. Effect of step density and orientation on the apparent pH dependence of hydrogen and hydroxide adsorption on stepped platinum surfaces. *J. Phys. Chem. C* **122**, 16756–16764 (2018).
9. Ledezma-Yanez, I. et al. Interfacial water reorganization as a pH-dependent descriptor of the hydrogen evolution rate on platinum electrodes. *Nat. Energy* **2**, 17031 (2017).
10. Seto, K., Iannelli, A., Love, B. & Lipkowski, J. The influence of surface crystallography on the rate of hydrogen evolution at Pt electrodes. *J. Electroanal. Chem. Interfacial Electrochem.* **226**, 351–360 (1987).
11. Marković, N. M., Sarraf, S. T., Gasteiger, H. A. & Ross, P. N. Hydrogen electrochemistry on platinum low-index single-crystal surfaces in alkaline solution. *J. Chem. Soc. Faraday Trans.* **92**, 3719–3725 (1996).
12. Marković, N., Grgur, B. & Ross, P. N. Temperature-dependent hydrogen electrochemistry on platinum low-index single-crystal surfaces in acid solutions. *J. Phys. Chem. B* **101**, 5405–5413 (1997).

13. Subbaraman, R. et al. Enhancing hydrogen evolution activity in water splitting by tailoring Li^+–$Ni(OH)_2$–Pt interfaces. *Science* **334**, 1256–1260 (2011).

14. Subbaraman, R. et al. Trends in activity for the water electrolyser reactions on 3*d* M(Ni,Co,Fe,Mn) hydr(oxy)oxide catalysts. *Nat. Mater.* **11**, 550–557 (2012).

15. Li, J. et al. Experimental proof of the bifunctional mechanism for the hydrogen oxidation in alkaline media. *Angew. Chem. Int. Ed.* **56**, 15594–15598 (2017).

16. Liu, E. et al. Unifying the hydrogen evolution and oxidation reactions kinetics in base by identifying the catalytic roles of hydroxyl–water–cation adducts. *J. Am. Chem. Soc.* **141**, 3232–3239 (2019).

17. Cong, Y. et al. Uniform $Pd_{0.33}Ir_{0.67}$ nanoparticles supported on nitrogen-doped carbon with remarkable activity toward the alkaline hydrogen oxidation reaction. *J. Mater. Chem. A* **7**, 3161–3169 (2019).

18. Qiu, Y. et al. BCC-phased PdCu alloy as a highly active electrocatalyst for hydrogen oxidation in alkaline electrolytes. *J. Am. Chem. Soc.* **140**, 16580–16588 (2018).

19. McCrum, I. T. & Koper, M. T. M. The role of adsorbed hydroxide in hydrogen evolution reaction kinetics on modified platinum. *Nat. Energy* **5**, 891–899 (2020).

20. Xue, S. et al. Influence of alkali metal cations on the hydrogen evolution reaction activity of Pt, Ir, Au, and Ag electrodes in alkaline electrolytes. *ChemElectroChem* **5**, 2326–2329 (2018).

21. Monteiro, M. C. O., Goyal, A., Moerland, P. & Koper, M. T. M. Understanding cation trends for hydrogen evolution on platinum and gold electrodes in alkaline media. *ACS Catal.* **11**, 14328–14335 (2021).

22. Weber, D., Janssen, M. & Oezaslan, M. Effect of monovalent cations on the HOR/HER activity for Pt in alkaline environment. *J. Electrochem. Soc.* **166**, F66–F73 (2019).

23. van der Niet, M. J. T. C., Garcia-Araez, N., Hernández, J., Feliu, J. M. & Koper, M. T. M. Water dissociation on well-defined platinum surfaces: the electrochemical perspective. *Catal. Today* **202**, 105–113 (2013).

24. Huang, B. et al. Cation- and pH-dependent hydrogen evolution and oxidation reaction kinetics. *JACS Au* **1**, 1674–1687 (2021).

25. Ding, M. et al. An on-chip electrical transport spectroscopy approach for in situ monitoring electrochemical interfaces. *Nat. Commun.* **6**, 7867 (2015).

26. Ding, M. et al. On-chip in situ monitoring of competitive interfacial anionic chemisorption as a descriptor for oxygen reduction kinetics. *ACS Cent. Sci.* **4**, 590–599 (2018).

27. Yoo, H.-W., Cho, S.-Y., Jeon, H.-J. & Jung, H.-T. Well-defined and high resolution Pt nanowire arrays for a high performance hydrogen sensor by a surface scattering phenomenon. *Anal. Chem.* **87**, 1480–1484 (2015).

28. Kiyohara, K. & Minami, R. Hydration and dehydration of monovalent cations near an electrode surface. *J. Chem. Phys.* **149**, 014705–014714 (2018).

29. Rebollar, L. et al. 'Beyond adsorption' descriptors in hydrogen electrocatalysis. *ACS Catal.* **10**, 14747–14762 (2020).

30. Mills, J. N., McCrum, I. T. & Janik, M. J. Alkali cation specific adsorption onto fcc(111) transition metal electrodes. *Phys. Chem. Chem. Phys.* **16**, 13699–13707 (2014).

31. Ringe, S. et al. Understanding cation effects in electrochemical CO_2 reduction. *Energy Environ. Sci.* **12**, 3001–3014 (2019).

32. Mähler, J. & Persson, I. A study of the hydration of the alkali metal Ions in aqueous solution. *Inorg. Chem.* **51**, 425–438 (2012).

33. McCrum, I. T. & Janik, M. J. First principles simulations of cyclic voltammograms on stepped Pt(553) and Pt(533) electrode surfaces. *ChemElectroChem* **3**, 1609–1617 (2016).

34. McCrum, I. T. & Janik, M. J. pH and alkali cation effects on the Pt cyclic voltammogram explained using density functional theory. *J. Phys. Chem. C.* **120**, 457–471 (2016).

35. Lust, E. in *Encyclopedia of Electrochemistry* (ed. Bard, A. J.) (Wiley, 2007); https://doi.org/10.1002/9783527610426.bard010204

36. Garlyyev, B., Xue, S., Watzele, S., Scieszka, D. & Bandarenka, A. S. Influence of the nature of the alkali metal cations on the electrical double-layer capacitance of model Pt(111) and Au(111) electrodes. *J. Phys. Chem. Lett.* **9**, 1927–1930 (2018).

37. Goyal, A. & Koper, M. T. Understanding the role of mass transport in tuning the hydrogen evolution kinetics on gold in alkaline media. *J. Chem. Phys.* **155**, 134705–134715 (2021).

38. Li, M. et al. Ultrafine jagged platinum nanowires enable ultrahigh mass activity for the oxygen reduction reaction. *Science* **354**, 1414–1419 (2016).

39. Adamo, C. & Barone, V. Toward reliable density functional methods without adjustable parameters: the PBE0 model. *J. Chem. Phys.* **110**, 6158–6170 (1999).

40. Kresse, G. & Joubert, D. From ultrasoft pseudopotentials to the projector augmented-wave method. *Phys. Rev. B* **59**, 1758–1775 (1999).

41. Kresse, G. & Furthmüller, J. Efficiency of ab-initio total energy calculations for metals and semiconductors using a plane-wave basis set. *Comput. Mater. Sci.* **6**, 15–50 (1996).

42. Kresse, G. & Furthmüller, J. Efficient iterative schemes for ab initio total-energy calculations using a plane-wave basis set. *Phys. Rev. B* **54**, 11169–11186 (1996).

43. Kresse, G. & Hafner, J. Ab initio molecular dynamics for liquid metals. *Phys. Rev. B.* **47**, 558–561 (1993).

44. Kresse, G. & Hafner, J. Ab initio molecular-dynamics simulation of the liquid-metal–amorphous-semiconductor transition in germanium. *Phys. Rev. B* **49**, 14251–14269 (1994).

45. Grimme, S., Antony, J., Ehrlich, S. & Krieg, H. A consistent and accurate ab initio parametrization of density functional dispersion correction (DFT-D) for the 94 elements H–Pu. *J. Chem. Phys.* **132**, 154104–1541023 (2010).

46. Yu, M. & Trinkle, D. R. Accurate and efficient algorithm for Bader charge integration. *J. Chem. Phys.* **134**, 064111–064119 (2011).

47. Steinmann, S. N., Michel, C., Schwiedernoch, R. & Sautet, P. Impacts of electrode potentials and solvents on the electroreduction of CO_2: a comparison of theoretical approaches. *Phys. Chem. Chem. Phys.* **17**, 13949–13963 (2015).

48. Chalk, S. J. The IUPAC Gold Book website (2019); https://doi.org/10.1351/goldbook.S05917

49. Humphrey, W., Dalke, A. & Schulten, K. VMD: visual molecular dynamics. *J. Mol. Graph.* **14**, 33–38 (1996).

50. Lu, T. Molclus program, version 1.9.9.2 (Beijing Kein Research Center for Natural Science, 2016).

51. Becke, A. D. Becke's three parameter hybrid method using the LYP correlation functional. *J. Chem. Phys.* **98**, 5648–5652 (1993).

52. Tirado-Rives, J. & Jorgensen, W. L. Performance of B3LYP density functional methods for a large set of organic molecules. *J. Chem. Theory Comput.* **4**, 297–306 (2008).

53. Schäfer, A., Huber, C. & Ahlrichs, R. Fully optimized contracted Gaussian basis sets of triple zeta valence quality for atoms Li to Kr. *J. Chem. Phys.* **100**, 5829–5835 (1994).

54. Frisch, M. et al. Gaussian 16, Revision C.01 (Gaussian, Inc., 2016).

55. Grimme, S., Ehrlich, S. & Goerigk, L. Effect of the damping function in dispersion corrected density functional theory. *J. Comput. Chem.* **32**, 1456–1465 (2011).

56. Lu, T. & Chen, F. Multiwfn: a multifunctional wavefunction analyzer. *J. Comput. Chem.* **33**, 580–592 (2012).

Acknowledgements

Author contributions

Competing interests

Additional information